

**CHARACTERIZATION OF DYNAMICS OF BINARY
GAS-SOLID FLOWS AND COAL GASIFICATION IN
FLUIDIZED BEDS: HIGH-SPEED IMAGING
MEASUREMENTS AND CFD SIMULATIONS**

SIRISHA PARVATHANENI



**DEPARTMENT OF CHEMICAL ENGINEERING
INDIAN INSTITUTE OF TECHNOLOGY DELHI
OCTOBER 2022**

© **Indian Institute of Technology Delhi (IITD), New Delhi, 2022**

**CHARACTERIZATION OF DYNAMICS OF BINARY
GAS-SOLID FLOWS AND COAL GASIFICATION IN
FLUIDIZED BEDS: HIGH-SPEED IMAGING
MEASUREMENTS AND CFD SIMULATIONS**

by

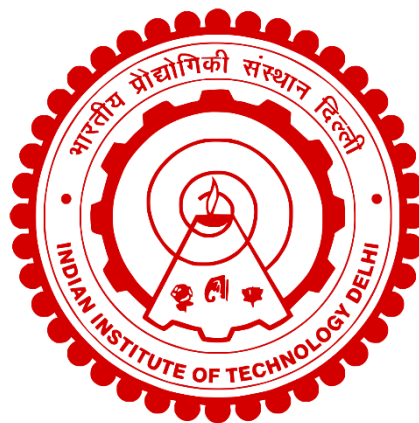
SIRISHA PARVATHANENI

Department of Chemical Engineering

Submitted

in fulfilment of the requirements of the degree of Doctor of Philosophy

to the



INDIAN INSTITUTE OF TECHNOLOGY DELHI

OCTOBER 2022

Certificate

This is to certify that the thesis entitled “**Characterization of Dynamics of Binary Gas-Solid Flows and Coal Gasification in Fluidized Beds: High-Speed Imaging Measurements and CFD Simulations**” is being submitted by **Ms. Sirisha Parvathaneni** to the **Indian Institute of Technology Delhi, New Delhi** for the award of the degree of **Doctor of Philosophy** is a bonafide record of original research work carried out by her under my supervision in conformity with rules and regulations of the Institute. The results contained in this thesis have not been submitted, in part or in full, to any other University or Institute for the award of any Degree or Diploma.

Date: 26 October 2022

Dr. Vivek V. Buwa

Professor

Department of Chemical Engineering,
Indian Institute of Technology Delhi,
New Delhi–110016, India.

**SUJAY
KARMAKAR**

Digitally signed by
SUJAY KARMAKAR
Date: 2022.10.26
18:07:54 +05'30'

Mr. Sujay Karmakar

General Manager,

Green Chemicals NETRA, NTPC Vindhyachal
Dist. Singrauli, MP-486885, India.

Acknowledgments

First and foremost, I am thankful to the universe for enabling me with strength, willpower, and good health to complete this research work and reach a platform to write this acknowledgment. I consider myself very fortunate to become a part of the Department of Chemical Engineering, IIT Delhi. I am forever grateful to IIT Delhi for providing me with the opportunity and ecosystem to carry out my research.

I express my heartfelt gratitude to my supervisor Prof. Vivek V. Buwa for his continuous encouragement, support, and guidance throughout my research work. His advice, suggestions, and rigorous scrutiny of my research work motivated me to do better and excel. I thank him for his diligence in shaping up my oral presentations and manuscripts which improved my oral and written communication skills to a great extent. I am also sincerely grateful to him for his support in other aspects of my life during my Ph.D.: to convert Ph.D. from full-time to part-time due to personal reasons, for his uninterrupted guidance during my part-time Ph.D. phase, and for suggestions on my career choices.

I am pleased to acknowledge my co-supervisor Mr. Sujay Karmakar from NTPC Energy Technology Research Alliance (NETRA) and Ph.D. research committee members, Prof. Shantanu Roy, Prof. P.M.V Subbarao, and Prof. Vikram Singh for their valuable suggestions and insightful feedback that helped to improve the quality of this research work.

I sincerely thank NETRA for providing the research fellowship. Also, I am grateful for the financial support received from IRD (IIT Delhi), DAAD, and NETRA for national and international travels for conferences and internship. The international travels to China and Europe have provided me an opportunity to interact with people from different research areas which improved my intellectual capacity and bolstered my confidence. These travels also exposed me to varied cultures and offered new perspectives on life.

I sincerely thank my present and ex-colleagues (Dr. Abhijeet, Sahil, Dr. David, Sayantani, Aniket, Dr. Ekta, Dr. Karthik, Sayantan, Vidit, Dr. Sanjeev, Dr. Brajesh, Siddhartha, Swapnil, Shivam, Kuldeep, Ankita, Sujata, Rohit, Devesh, Rajneesh, and Dr. Abdul) for lending their support on research-related activities and sharing their knowledge through technical discussions, which broadened my knowledge on different research areas. I owe special thanks to Abhijeet, Sahil, David, Sayantani, and hostel mate Richa for the moral and emotional support in different stages at and outside research work, and also for making the life at IIT Delhi cheerful. I also thank Anil for his assistance in assembling experimental set-ups and administrative related activities during my tenure at IIT Delhi

Lastly and most importantly, I am always grateful to my parents for their unconditional love, support, sacrifice, and persistent encouragement in different stages of my educational career. I am thankful to my husband, sister, brother-in-law, and niece for making work from home due to the COVID pandemic joyful.

Thanks again to all for the support and encouragement.



26 October 2022

Sirisha Parvathaneni

Abstract

Gas-solids fluidized beds are widely used in several industrial processes like coal/biomass gasification and/or combustion, catalytic polymerization, etc. These industrial processes often involve fluidizing/defluidizing of a mixture of particles that differ in size or density or shape, e.g., fluidizing of coal/biomass and inerts in the gasification process, and defluidizing of different-sized polymer particles in catalytic polymerization. Therefore, the performance of these industrial processes is predominantly influenced by the spatial distribution of solid phases which is primarily governed by the local bubbling behavior. Depending on the particle size/density ratios and operating superficial gas velocities (U_G), the bubble carries lesser dense/bigger size particles with it leading to segregation of higher dense/smaller size particles. Such different segregation and mixing mechanisms should be predicted accurately by the CFD models. Such models can be further extended to simulate the industrial-scale fluidized bed reactors. Since the flow is inherently unsteady the CFD models should be validated with time- and space-resolved measurements.

In the present work, the dynamics of the binary gas-solids flows with particles differing in density or size or both in a pseudo-2D rectangular fluidized bed is characterized using high-speed imaging measurements. The bubbling characteristics were controlled using three different modes of air injection: uniform, two-jet, and single-jet distributors under the same U_G . The local individual phase area fraction fluctuations of all three phases (air and two solids) were measured. These measurements were further used to quantify the effects of particle size/density ratio, bed composition, mode of air injection, and U_G on the bubbling characteristics (bubble size distribution and local bubbling frequency) and eventually on the dynamics of segregation/ mixing. These measurements form a crucial database for the validation of Eulerian multi-fluid and CFD-DEM models which is the other objective of the present work.

The multi-fluid Eulerian simulations were performed for binary mixtures varying in size and/or density ratios, bed composition, U_G , and modes of gas injection. The results show that the models/parameters (gas-solid drag, solids frictional pressure, and specular coefficient) that predicted the bubbling/spouting behavior of corresponding unary gas-solids flows correctly, predicted the bubbling/spouting behavior and dynamics of segregation of binary gas-solids flow accurately. Further, the roles of different forces (gas-particle drag, particle-particle drag, and solids viscosities) on the kinetic energies of the solid phases and ultimately on certain segregation and mixing mechanisms were quantified. The present work provides a detailed understanding of the flow physics for different operating parameters i.e., mode of gas injection, particle size/density ratios, bed composition, and U_G on local spouting/bubbling behavior and eventually on dynamics of segregation/mixing. Furthermore, in the coal gasification process, the effect of different local bubbling behaviors on the segregation/mixing of coal and inert solid phases and ultimately on reaction mechanisms, syngas composition, and syngas quality was quantified.

सार

गैस-ठोस द्रवित बेड का व्यापक रूप से कई औद्योगिक प्रक्रियाओं जैसे कोयला / बायोमास गैसीकरण और / या दहन, उत्प्रेरक पोलीमराइजेशन, आदि में उपयोग किया जाता है। इन औद्योगिक प्रक्रियाओं में अक्सर कणों के मिश्रण का द्रवीकरण / डिफ्लुइडाइजिंग शामिल होता है जो आकार या घनत्व या आकार में भिन्न होते हैं, उदा। , गैसीकरण प्रक्रिया में कोयले/बायोमास और अक्रिय का द्रवीकरण, और उत्प्रेरक पोलीमराइजेशन में विभिन्न आकार के बहुलक कणों का द्रवीकरण। इसलिए, इन औद्योगिक प्रक्रियाओं का प्रदर्शन मुख्य रूप से ठोस चरणों के स्थानिक वितरण से प्रभावित होता है जो मुख्य रूप से स्थानीय बुदबुदाती व्यवहार द्वारा नियंत्रित होता है। कण आकार/घनत्व अनुपात और ऑपरेटिंग सतही गैस वेग (यूजी) के आधार पर, बुलबुले में कम घने/बड़े आकार के कण होते हैं जिससे उच्च घने/छोटे आकार के कणों का पृथक्करण होता है। सीएफडी मॉडल द्वारा इस तरह के अलग-अलग अलगाव और मिश्रण तंत्र की सटीक भविष्यवाणी की जानी चाहिए। औद्योगिक पैमाने पर द्रवीकृत बिस्तर रिएक्टरों का अनुकरण करने के लिए इस तरह के मॉडल को और बढ़ाया जा सकता है। चूंकि प्रवाह स्वाभाविक रूप से अस्थिर है, इसलिए सीएफडी मॉडल को समय और स्थान-समाधान माप के साथ मान्य किया जाना चाहिए।

वर्तमान कार्य में, बाइनरी गैस-ठोस की गतिशीलता घनत्व या आकार में भिन्न कणों के साथ बहती है या दोनों एक छद्म -2 डी आयताकार द्रवित बिस्तर में उच्च गति इमेजिंग माप का उपयोग करने की विशेषता है। बुदबुदाती विशेषताओं को वायु इंजेक्शन के तीन अलग-अलग तरीकों का उपयोग करके नियंत्रित किया गया था: एक ही यूजी के तहत वर्दी, दो-जेट और एकल-जेट वितरक। सभी तीन चरणों (वायु और दो ठोस) के स्थानीय व्यक्तिगत चरण क्षेत्र अंश के उतार-चढ़ाव को मापा गया। इन मापों का उपयोग कण आकार/घनत्व अनुपात, बिस्तर संरचना, वायु इंजेक्शन के तरीके, और बुदबुदाहट विशेषताओं (बुलबुला आकार वितरण और स्थानीय बुदबुदाहट आवृत्ति) पर और अंततः अलगाव/मिश्रण की गतिशीलता पर प्रभाव को मापने के लिए किया गया था। ये माप यूलेरियन मल्टी-फ्लुइड और

सीएफडी-डीईएम मॉडल के सत्यापन के लिए एक महत्वपूर्ण डेटाबेस बनाते हैं जो वर्तमान कार्य का अन्य उद्देश्य है।

बहु-द्रव यूलेरियन सिमुलेशन आकार और / या घनत्व अनुपात, बिस्तर संरचना, यूजी, और गैस इंजेक्शन के तरीकों में भिन्नता वाले बाइनरी मिश्रण के लिए किए गए थे। परिणाम बताते हैं कि मॉडल/पैरामीटर (गैस-सॉलिड ड्रैग, सॉलिड फ्रिक्शनल प्रेशर, और स्पेक्युलरिटी गुणांक) जिसने संबंधित यूनरी गैस-सॉलिड्स के बुदबुदाहट/स्पाउटिंग व्यवहार की भविष्यवाणी की थी, सही ढंग से बहती है, बुदबुदाती/स्पाउटिंग व्यवहार और बाइनरी के अलगाव की गतिशीलता की भविष्यवाणी की थी। गैस-ठोस प्रवाह सही ढंग से। इसके अलावा, ठोस चरणों की गतिज ऊर्जाओं पर और अंततः कुछ अलगाव और मिश्रण तंत्र पर विभिन्न बलों (गैस-कण ड्रैग, कण-कण ड्रैग, और ठोस चिपचिपाहट) की भूमिकाएं निर्धारित की गईं। वर्तमान कार्य विभिन्न ऑपरेटिंग मापदंडों के लिए प्रवाह भौतिकी की एक विस्तृत समझ प्रदान करता है, अर्थात् गैस इंजेक्शन का तरीका, कण आकार / घनत्व अनुपात, बिस्तर संरचना, और स्थानीय स्पाउटिंग / बबलिंग व्यवहार पर यूजी और अंततः अलगाव / मिश्रण की गतिशीलता पर। इसके अलावा, कोयला गैसीकरण प्रक्रिया में, कोयले और अक्रिय ठोस चरणों के पृथक्करण/मिश्रण पर और अंततः प्रतिक्रिया तंत्र, सिनगैस संरचना और सिनगैस गुणवत्ता पर विभिन्न स्थानीय बुदबुदाहट व्यवहारों का प्रभाव निर्धारित किया गया था।

Contents

Certificate.....	i
Acknowledgments.....	ii
Abstract.....	iv
Contents	viii
List of Figures	xi
List of Tables	xix
Nomenclature.....	xx
Chapter 1: Introduction	1
1. Introduction	2
1.1 Objectives	6
1.2 Organization of thesis	6
Chapter 2: Experimental Investigations of Segregation and Mixing of Binary Gas-Solids Flows of Particles with Different Density *	10
2.1 Introduction	11
2.2 Experimental set-up.....	14
2.3 Digital image processing methodology.....	15
2.3.1 Identification of individual solid phases	16
2.3.2 Identification of bubbles	19
2.4 Results and Discussion.....	20
2.4.1 Dynamics of segregation of binary mixtures	27
2.4.1.1 Effect of mixture composition on segregation.....	27
2.4.1.2 Effect of bubbling behavior on segregation.....	37
2.4.2 Dynamics of mixing behavior of binary mixtures	39
2.5 Summary and Conclusions.....	41
Chapter 3: Eulerian Simulations of Bubbling and Jetting Regimes in a Fluidized bed.....	44
3.1 Introduction	45
3.2 Methodology	48
3.2.1 Measurements	48
3.2.2 Computational model.....	49
3.2.2.1 Numerical solution, boundary conditions	55
3.2.2.2 Data post-processing.....	56
3.2.2.3 Effect of grid resolution on bubbling characteristics.....	57
3.3 Results and Discussion.....	58
3.3.1 Effect of gas-solid drag on bubbling characteristics.....	59

3.3.2 Effect of solid frictional pressure on bubbling characteristics.....	64
3.3.3 Effect of gas distributor on jetting behavior	73
3.4 Summary and Conclusions.....	80
Chapter 4: Eulerian Multifluid Simulations of Segregation and Mixing of Binary Gas-Solids Flows of Particles with Different Densities*	83
4.1 Introduction	84
4.2 Methodology	88
4.2.1 Measurements	88
4.2.2 Computational model.....	89
4.2.2.1 Governing equations	89
4.2.2.2 Initial packing limit of solid phases	90
4.2.2.3 Quantification of segregation and mixing.....	91
4.3 Results and Discussion.....	92
4.3.1 Effect of polydisperse kinetic theory on dynamics of segregation	92
4.3.2 Effect of particle-particle drag on the dynamics of segregation	95
4.3.3 Effect of bubbling behavior on dynamics of segregation	104
4.3.4 Effect of U_G on dynamics of mixing.....	107
4.3.5 Effect of bed composition on dynamics of segregation.....	110
4.4. Summary and Conclusions.....	115
Chapter 5: Effect of Bubbling/Spouting Behavior on Dynamics of Segregation of Particles with Different Size and Density Ratios	118
5.1 Introduction	119
5.2 Methodology	122
5.2.1 Measurements	122
5.2.2 Computational model.....	124
5.2.2.1 Initial and maximum packing limit of solid phases	126
5.2.3 Quantification of segregation and mixing.....	127
5.2.4 Effect of grid resolution and time-step on dynamics of binary gas-solids flow ...	128
5.3 Results and Discussion.....	129
5.3.1 Effect of spouting behavior on dynamics of segregation.....	130
5.3.2 Effect of mode of gas-injection on dynamics of segregation	141
5.3.3 Effect of bed composition and bubbling/spouting behavior on segregation dynamics	143
5.3.4 Effect of particle size/density ratios on the dynamics of segregation.....	150
5.3.4.1 Binary mixture differing in size	150
5.3.4.2 Binary mixture differing in size and density.....	156

5.4 Summary and Conclusions.....	159
Chapter 6: Effect of Bubbling Behavior on Performance of Fluidized Bed Gasifier	162
6.1 Introduction	163
6.2 Fluidized bed gasifier measurements	166
6.3 Computational methodology	167
6.3.1 Governing equations	167
6.3.2 Coal gasification kinetics	171
6.3.3 Simulation set-up, boundary conditions, and numerical schemes	173
6.3.4 Grid-size study	174
6.4 Results and Discussion.....	176
6.4.1 Validation of the model	176
6.4.2 Effect of local bubbling behavior on hydrodynamics.....	177
6.4.3 Reaction mechanisms and species distributions	182
6.4.4 Effect of bubbling behavior on syngas quality	190
6.4.5 Effect of inlet mass flow rates on bubbling behavior and syngas composition....	192
6.5 Conclusions	194
Chapter 7: Summary and Conclusions.....	197
7.1 Summary	198
7.2 Conclusions	199
7.3 Suggestions for future work	202
References.....	204
Scientific Contributions	215
Biosketch.....	217

List of Figures

Figure 1.1: Schematic of fluidized beds used for (a) biomass/coal gasification [1], (b) polymerization [2], and (c) drying in pharmaceutical industries [3]	2
Figure 1.2: Schematic of coal gasification in fluidized bed.....	3
Figure 2.1: Schematic of the experimental set-up	16
Figure 2.2: (i) Greyscale image (ii) histogram of the colour intensity of the image and (iii) converted RGB image for (a) only GB, (b) only SAGO, (c) only air, and (d) 70 GB–30 SAGO mixture fluidized using uniform distributor at $Q_G = 25 \text{ m}^3/\text{h}$	17
Figure 2.3: Effect of (a) GB cut-off value and (b) air cut-off value on the time evolution of A_{SAGO} (70 GB–30 SAGO, $U_G = 1.736 \text{ m/s}$, uniform distributor).....	18
Figure 2.4: Bubble identification methodology for 70 GB–30 SAGO fluidized using the uniform distributor at $U_G = 1.736 \text{ m/s}$ (a) cropped greyscale image, (b) bubble regions smeared by applying filters, (c) identified bubbles (d) converted into RGB image (original greyscale), and (e) image after subtraction of bubbles	20
Figure 2.5: Effect of U_G on time-evolution of the solid dispersion height (h_s)	21
Figure 2.6: Effect of U_G and composition on the solids dispersion height.....	22
Figure 2.7: Effect of the U_G on segregation/mixing behavior of binary mixture 70 GB–30 SAGO fluidized using the uniform distributor at U_G of (a) 1.736 m/s, (b) 2.083 m/s, (c) 2.43 m/s, and (d) 2.78 m/s.....	24
Figure 2.8: Effect of U_G on time-evolution of mixing index for binary mixture 70 GB–30 SAGO fluidized using uniform distributor	25
Figure 2.9: Reproducibility of time-evolution of mixing index for binary mixture 70 GB–30 SAGO fluidized using uniform distributor at $U_G = 1.736 \text{ m/s}$	26
Figure 2.10: Reproducibility of time-evolution of individual phase area fraction fluctuations for binary mixture 70 GB–30 SAGO.....	27
Figure 2.11: Effect of bubbling behaviour on segregation of 70 GB–30 SAGO binary mixture fluidized using (a) uniform and (b) two-jet distributor at $U_G = 1.736 \text{ m/s}$	28
Figure 2.12: Effect of bubbling behavior on segregation of 50 GB–50 SAGO binary mixture fluidized using (a) uniform and (b) two-jet distributor at $U_G = 1.736 \text{ m/s}$	29
Figure 2.13: Effect of bubbling behavior on segregation of 30 GB–70 SAGO binary mixture fluidized using (a) uniform and (b) two-jet distributor at $U_G = 1.736 \text{ m/s}$	29
Figure 2.14: Effect of type of gas-distributor on time-evolution of area fraction of individual phases in case of (a) uniform and (b) two-jet distribution (70 GB–30 SAGO, $U_G = 1.736 \text{ m/s}$, location P_1 : $x = 15 \text{ cm}$, $y = 5 \text{ cm}$, $z = 2 \text{ cm}$)	31
Figure 2.15: Effect of type of gas-distributor on time-evolution of area fraction of individual phases in case of (a) uniform and (b) two-jet distribution (50 GB–50 SAGO, $U_G = 1.736 \text{ m/s}$, location P_1 : $x = 15 \text{ cm}$, $y = 5 \text{ cm}$, $z = 2 \text{ cm}$)	32
Figure 2.16: Effect of type of gas-distributor on time-evolution of area fraction of individual phases in case of (a) uniform and (b) two-jet distribution ($x = 15 \text{ cm}$, $y = 5 \text{ cm}$, 30 GB–70 SAGO, $U_G = 1.736 \text{ m/s}$, location P_1 : $x = 15 \text{ cm}$, $y = 5 \text{ cm}$, $z = 2 \text{ cm}$).....	33
Figure 2.17: Effect of bed composition on time-evolution of the mixing index for binary mixtures fluidized using (a) uniform and (b) two-jet distributor at $U_G = 1.736 \text{ m/s}$	34

Figure 2.18: Time evolution of individual phases area fraction of (a) 100 GB–0SAGO and (b) 0 GB–100 SAGO (uniform distributor, $U_G = 1.736$ m/s, location P_2 : $x = 15$ cm, $y = 5$ cm, $z = 2$ cm)	34
Figure 2.19: Time evolution of individual phases area fraction of (a) 100 GB–0SAGO and (b) 0 GB–100 SAGO (uniform distributor, $U_G = 1.736$ m/s, location P_2 : $x = 10$ cm, $y = 15$ cm, $z = 2$ cm)	35
Figure 2.20: Effect of composition on time-evolution of area fraction of individual phases for (a) (b) 70 GB–30 SAGO, (c) 50 GB–50 SAGO, (d) 30 GB–70 SAGO (uniform distributor, $U_G = 1.736$ m/s, location P_2 : $x = 10$ cm, $y = 15$ cm, $z = 2$ cm).....	35
Figure 2.21: Effect of gas distributor on bubble size distribution for (a) uniform and (b) two-jet distributor at $U_G = 1.736$ m/s	36
Figure 2.22: Effect of gas distributor on power spectra of local bubble area fraction fluctuations (a) uniform and (b) two-jet distributor ($U_G = 1.736$ m/s, location: P_1 ($x = 15$ cm, $y = 5$ cm, $z = 2$ cm)).....	36
Figure 2.23: Effect of composition on time-evolution of area fraction of individual phases for (a) 70 GB–30 SAGO, (b) 50 GB–50 SAGO, and (c) 30 GB–70 SAGO (uniform distributor, $U_G = 2.78$ m/s, location P_1 : $x = 15$ cm, $y = 5$ cm, $z = 2$ cm).....	40
Figure 2.24: Effect of bed composition on time-evolution of the mixing index for binary gas-solids flow at $U_G = 2.78$ m/s (uniform distributor)	41
Figure 2.25: Effect of mixture composition on bubble size distribution at $U_G = 2.78$ m/s	41
Figure 2.26: Effect of mixture composition on power spectra of local gas-phase area fraction fluctuations (uniform distributor, $U_G = 2.78$ m/s, location P_1 : $x = 15$ cm, $y = 5$ cm, $z = 2$ cm)	41
Figure 3.1: Solution domain and mesh (uniform distributor)	56
Figure 3.2: Identification of bubble from (a) predicted volume fraction distribution of air and (b) binarized image (unary SAGO, $U_G = 1.736$ m/s).....	57
Figure 3.3: Effect of the grid resolution on the predicted (a) time-averaged axial α_s , (b) bubble size distribution, and (c) power spectra of local gas-phase area fraction fluctuations at 15 cm from the distributor (Unary SAGO, $U_G = 1.736$ m/s).....	58
Figure 3.4: Effect of the gas-solid drag model on the gas-solid momentum exchange coefficient as a function of slip velocity and volume fraction of gas for gas-solid drag model of (a) Gidaspow [66], (b) Singh et al. [42], (c) Li & Yang [67], and (d) Gibilaro et al. [68]..	60
Figure 3.5: Effect of the gas-solid drag model on the predicted solids dispersion height for (a) unary GB and (b) unary SAGO (uniform distributor)	61
Figure 3.6: Comparison of measured and predicted time-evolution of the local gas-phase area fraction fluctuations using different gas-solid drag models (unary GB , $U_G = 1.736$ m/s, 5 cm from air distributor, uniform distributor)	62
Figure 3.7: Comparison of measured and predicted time-evolution of the local gas-phase area fraction fluctuations using different gas-solid drag models (unary SAGO , $U_G = 2.78$ m/s, 5 cm from air distributor, uniform distributor)	63
Figure 3.8: Effect of gas-solid drag model on the bubble size distribution for (a) unary GB at U_G of 1.736 m/s and (b) unary SAGO at U_G of 2.78 m/s (uniform distributor)	63
Figure 3.9: Effect of (a) KTGF- P_s , f , $\phi = 0.05$, (b) J&J- P_s , f , $\phi = 0.05$, and (c) J&J- P_s , f , $\phi = 0.5$ on the predicted (i) α_s distribution, (ii) μ_s , f_r , (iii) solids velocity distribution at center plane, (iv) solids velocity at wall, and (v) wall shear stress (unary GB , $U_G = 1.736$ m/s, uniform distributor).....	65

Figure 3.10: Effect of the model for Ps, f and value for ϕ on the time-evolution of the total solids frictional viscosity for (a) unary GB at U_G of 1.736 m/s, unary SAGO at U_G of (b) 1.736 m/s and (c) 2.78 m/s (uniform distributor).....	66
Figure 3.11: Effect of the model for Ps, f and value for ϕ on the time-evolution of the total solids velocity for (a) unary GB at U_G of 1.736 m/s, unary SAGO at U_G of (b) 1.736 m/s and (c) 2.78 m/s (uniform distributor)	67
Figure 3.12: Comparison of measured and predicted time-evolution of the local gas-phase area fraction fluctuations using different Ps, f models and ϕ values at (a) 5 cm and (b) 15 cm from the distributor (unary GB , $U_G = 1.736$ m/s, uniform distributor)	67
Figure 3.13: Effect of Ps, f model and ϕ value on bubble size distribution for unary GB at U_G of 1.736 m/s (uniform distributor)	68
Figure 3.14: Effect of the value for ϕ on the distribution of wall shear stress ($t = 40$ s) in entire domain for (a) unary GB at U_G of 1.736 m/s, unary SAGO at U_G of (b) 1.736 m/s and (c) 2.78 m/s (uniform distributor)	69
Figure 3.15: Effect of frictional pressure models and wall boundary conditions on the bubble velocity (unary GB , $U_G = 1.736$ m/s, uniform distributor).....	70
Figure 3.16: Effect of frictional viscosity model and wall boundary condition on the bubble diameter along with the bed height (unary GB , $U_G = 1.736$ m/s, uniform distributor).....	71
Figure 3.17: Effect of Ps, f model and ϕ value on bubble size distribution for unary SAGO at (a) U_G of 1.736 m/s and (b) U_G of 2.78 m/s (uniform distributor).....	73
Figure 3.18: Effect of the gas-solid drag model of (i) Gidaspow [66], (ii) Gibilaro et al. [68], and (iii) Li & Yang [68] on the instantaneous (a) volume fraction distribution of solid (α_s), (b) βgs , (c) velocity of solids, and (d) measurements (Solid: dark grey, Air: light grey) (unary GB , $U_G = 1.736$ m/s, two-jet distributor).....	74
Figure 3.19: Effect of the gas-solid drag model of (i) Gidaspow [66], (ii) Gibilaro et al. [68], and (iii) Li & Yang [68] on the instantaneous (a) volume fraction distribution of solid (α_s), (b) βgs , (c) velocity of solids, and (d) measurements (Solid: dark grey, Air: light grey) (unary SAGO , $U_G = 1.736$ m/s, two-jet distributor)	75
Figure 3.20: Effect of the gas-solid drag force of (i) Gidaspow [66], (ii) Gibilaro et al. [68], and (iii) Li & Yang [68] on the predicted volume fraction distribution of solid phase and (iv) measurements for unary GB at U_G of (a) 2.083 m/s, (b) 2.78 m/s and (c) unary SAGO at U_G of 2.78 m/s (two-jet distributor).....	78
Figure 3.21: Effect of the gas-solid drag model on the predicted solids dispersion height for (a) unary GB and (b) unary SAGO (two-jet distributor)	79
Figure 3.22: Effect of the mode of gas-injection of (i) uniform distributor and (ii) two-jet distributor on velocity distribution of solid phase for (a) unary GB, $U_G = 1.736$ m/s, (b) unary GB, $U_G = 2.083$ m/s, and (c) unary SAGO, $U_G = 1.736$ m/s	80
Figure 4.1: Different mechanisms of particle-particle momentum exchange due to particle collisions and momentum exchange between the solid phases is accounted due to (a) fluid-dynamic velocity difference, (b) fluid-dynamic and peculiar velocity differences, and due to continuous particle contacts under dense bed conditions (c) short-term and (d) long-term interactions (Particles with different color indicate particles with different physical properties: density or size, yellow: solid phase fluid-dynamic velocity, blue: solid phase peculiar or fluctuating velocity)	86
Figure 4.2: Comparison of volume fraction distribution of (a) GB, (b) SAGO, and (c) air predicted using different kinetic theories of (i) mono-disperse kinetic theory with $Psit$	

extended for polydisperse flows, polydisperse kinetic theories of (ii) Chao et al. [18], (iii) Mathiesen et al. [116], and (d) measurements (GB: Black, SAGO: Green, air: Red).....	93
Figure 4.3: Comparison of measured and predicted time-evolution of mixing index using (a) different kinetic theories and (b) different kinetic theories with same particle-particle drag model of Syamlal [70] (70 GB–30 SAGO, $U_G = 1.736$ m/s)	94
Figure 4.4: Effect of particle-particle drag model of (a) Syamlal [70], (b) Chao et al. [11], and (c) modified Chao et al. [11] (present work) on the prediction of (i) α_s of GB, (ii) α_s of SAGO, (iii) β_{pec} , (iv) β_{hyd} , (v) β_{fri} , (vi) β_{s1s2} , (vii) Pst of GB, and (viii) Pst of SAGO (70 GB–30 SAGO, $U_G = 1.736$ m/s, $t = 10$ s).....	97
Figure 4.5: Comparison of the cumulative total particle-particle drag coefficient predicted using particle-particle drag models of (a) modified Chao et al. [11] and (b) Chao et al. [11]	98
Figure 4.6: Comparison of time-evolution of cumulative total particle-particle drag force magnitude predicted using different particle-particle drag models	99
Figure 4.7: Comparison of α_s distribution of GB and SAGO predicted using particle-particle drag models of (a) Syamlal [70], (b) Chao et al. [11], (c) modified Chao et al. [11] (present work), and (d) measurements (GB: Black, SAGO: Green, air: Red)	101
Figure 4.8: Comparison of measured and predicted time-evolution of mixing index using different particle-particle drag models (70 GB–30 SAGO, $U_G = 1.736$ m/s).....	101
Figure 4.9: Comparison of the time-evolution of predicted total drag forces using modified Chao et al. [11] drag model (70 GB–30 SAGO, $U_G = 1.736$ m/s).....	102
Figure 4.10: Effect of the kinetic theory model on time-evolution of mixing index with particle-particle drag model of modified Chao et al. [11]	102
Figure 4.11: Effect of Ps, f models and ϕ values on the prediction of time-evolution of cumulative GB phase (a) viscosity and (b) velocity (70 GB–30 SAGO, $U_G = 1.736$ m/s, modified Chao et al. [11] drag).....	105
Figure 4.12: Comparison of measured and predicted time-evolution of local gas-phase area fraction fluctuations at 5 cm from distributor using different Ps, f models and ϕ values (70 GB–30 SAGO, $U_G = 1.736$ m/s, modified Chao et al. [11] drag)	106
Figure 4.13: Effect of Ps, f models, and ϕ values on the (a) bubble size distribution and (b) local bubbling frequency at 5 cm from distributor	106
Figure 4.14: Comparison of (a) measured (GB: Black, SAGO: Green, air: Red) and predicted α_s of GB using (b) J&J- Ps, f model, $\phi_{GB-WALL}$ of 0.5, and (c) KTGF- Ps, f model, $\phi_{GB-WALL}$ of 0.05 at U_G of 1.736 m/s (70 GB–30 SAGO, modified Chao et al. [11] drag).....	107
Figure 4.15: Effect of Ps, f models, and ϕ values on the prediction of time-evolution of mixing index (70 GB–30 SAGO, $U_G = 1.736$ m/s, modified Chao et al. [11] drag).....	107
Figure 4.16: Predicted time-evolution of cumulative drag forces at U_G of 2.78 m/s (70 GB–30 SAGO, modified Chao et al. [11] drag).....	108
Figure 4.17: Comparison of measured and predicted local gas-phase area fraction fluctuations at 5 cm from distributor at $U_G = 2.78$ m/s (70 GB–30 SAGO, modified Chao et al. [11] drag)	108
Figure 4.18: Comparison of (a) measured (GB: Black, SAGO: Green, air: Red) and predicted volume fraction distribution of (b) GB and (c) air at U_G of 2.78 m/s (70 GB–30 SAGO, modified Chao et al. [11] drag).....	109
Figure 4.19: Comparison of measured and predicted time-evolution of mixing index at U_G of 2.78 m/s (70 GB–30 SAGO, $U_G = 2.78$ m/s).....	109

Figure 4.20: Effect of the particle-particle drag on the prediction of the time-evolution of the mixing index for $\beta s1s2$ model of (a) modified Chao et al. [11]) and (b) modified Chao et al. [11]with correction factor at $U_G = 1.736$ m/s	110
Figure 4.21: Distribution of particle-particle drag correction factor $\alpha_s, GB_{local}\alpha_s, GB$ for different bed compositions of (a) 70 GB–30 SAGO, (b) 50 GB–50 SAGO, and (c) 30 GB–70 SAGO at U_G of 1.736 m/s.....	112
Figure 4.22: Comparison of the time-evolution of the total particle-particle drag force magnitude with and without the correction factor for different bed compositions of (a) 70 GB–30 SAGO, (b) 50 GB–50 SAGO, and (c) 30 GB–70 SAGO ($U_G = 1.736$ m/s).....	113
Figure 4.23: Effect of bed composition on the instantaneous volume fraction distribution of (a) air, (b) GB, and (c) measurements (GB: Black, SAGO: Green, air: Red) for binary mixture of (i) 70 GB–30 SAGO, (ii) 50 GB–50 SAGO, and (iii) 30 GB–70 SAGO	114
Figure 4.24: Effect of the bed composition on the local gas-phase area fraction fluctuations at 5 cm from air distributor for the binary mixtures of (a) 70 GB–30 SAGO, (b) 50 GB–50 SAGO, and (c) 30 GB–70 SAGO (modified Chao et al. [11] with correction factor $U_G = 1.736$ m/s)	114
Figure 4.25: Effect of the bed composition on the bubble size distribution (a) measurements and (b) simulation for the binary mixture of (i) 70 GB–30 SAGO, (ii) 50 GB–50 SAGO, and (c) 30 GB–70 SAGO at U_G of 1.736 m/s	115
Figure 5.1: Identification of height of segregated GB922 layer for 70 GB922–30 GB96 binary mixture (a) cropped grey scale image (Black: GB922, Grey: GB96, White: Air) and (b) binarized image	124
Figure 5.2: Identification of height of segregated GB922 layer for 70 GB922–30 GB96 (a) predicted volume fraction distribution of GB922 and (b) binarized image.....	127
Figure 5.3: Effect of (a) grid resolution ($\Delta t = 0.0001$ s) and (b) time-step (medium grid) on time-evolution of mixing index of 30 GB2267–70 SAGO binary mixture (Two-jet distributor, $U_G = 1.736$ m/s)	128
Figure 5.4: Effect of the $\beta_{air} - GB2267$ model of (a) Gidaspow [66], (b) Gibilaro et al. [68], and (c) modified drag on the magnitude of gas-solid momentum exchange coefficient (70 GB2267–30 SAGO, two-jet distributor, $U_G = 1.736$ m/s)	131
Figure 5.5: Effect of the $\beta_{air} - GB$ model of (a) Gidaspow [66], (b) Gibilaro et al. [68], and (c) modified drag on the distribution of K.E of GB2267 for binary mixture of 70 GB2267–30 SAGO (Two-jet distributor, $U_G = 1.736$ m/s).....	132
Figure 5.6: Effect of the $\beta_{air} - GB$ model of (a) Gidaspow [66], (b) Gibilaro et al. [68], and (c) modified-drag on the volume fraction distribution of (a) air, (b) GB2267, and (c) measurement (GB: Black, SAGO: Green, air: Red) for binary mixture of 70 GB2267–30 SAGO (Two-jet distributor, $U_G = 1.736$ m/s)	134
Figure 5.7: Effect of the $\beta_{air} - GB$ model on the time-evolution of the mixing index for (a) 70 GB2267–30 SAGO, (b) 50 GB2267–50 SAGO, and (c) 30 GB2267–70 SAGO mixtures (Two-jet distributor, $U_G = 1.736$ m/s).....	135
Figure 5.8: Effect of the $\beta_{air} - GB$ model of (a) Gidaspow [66], (b) Gibilaro et al. [68], and (c) modified-drag on the volume fraction distribution of (a) air, (b) GB2267, and (c) measurement (GB: Black, SAGO: Green, air: Red) for binary mixture of 50 GB2267–50 SAGO (Two-jet distributor, $U_G = 1.736$ m/s)	136

Figure 5.9: Effect of $\beta_{air} - GB$ model of (a) Gidaspow [66], (b) Gibilaro et al. [68], and (c) modified drag on the distribution of K.E of GB2267 for binary mixture of 50 GB2267–50 SAGO (Two-jet distributor, $U_G = 1.736$ m/s)	136
Figure 5.10: Effect of the $\beta_{air} - GB$ model of (a) Gidaspow [66], (b) Gibilaro et al. [68], and (c) modified-drag on the volume fraction distribution of (a) air, (b) GB2267, and (c) measurement (GB: Black, SAGO: Green, air: Red) for binary mixture of 30 GB2267–70 SAGO (Two-jet distributor, $U_G = 1.736$ m/s)	137
Figure 5.11: Comparison of (i) measured (GB22672: Black, SAGO: Green, Red: air) and (ii) predicted volume fraction distribution of GB2267 at U_G of (a) 2.083 m/s and (b) 2.78 m/s (70 GB2267–30 SAGO, modified Chao et al. [11] drag, uniform distributor).....	137
Figure 5.12: Effect of the gas-solid drag model of (i) modified Gibilaro et al. [68] and (ii) Li and Yang [67] on the prediction of volume fraction distribution of (a) gas phase, (b) GB2267, and (c) measurements (Black: GB2267, Green: SAGO, Red: Air)	138
Figure 5.13: Effect of the gas-solid drag model of (i) modified Gibilaro et al. [68] and (ii) Li and Yang [67] on the prediction of volume fraction distribution of (a) gas phase, (b) GB2267, and (c) measurements (Black: GB2267, Green: SAGO, Red: Air)	140
Figure 5.14: Effect of the gas-solid drag model on the time-evolution of the mixing index at U_G of (a) 2.083 m/s and (b) 2.78 m/s (70 GB2267–30 SAGO, Two-jet distributor)	140
Figure 5.15: Effect of $\beta_{air} - GB$ model of (a) Gidaspow [66], (b) Gibilaro et al. [68], and (c) modified drag on the distribution of K.E of GB2267 for binary mixture of 50 GB2267–50 SAGO (Two-jet distributor, $U_G = 1.736$ m/s)	141
Figure 5.16: Effect of the mode of gas injection on the kinetic energy per unit mass (m^2/s^2) of GB2267 with (i) uniform, (ii) two-jet, and (iii) single-jet gas distributor for binary mixtures of (a) 30 GB2267–70 SAGO, (b) 50 GB2267–50 SAGO, and (c) 70 GB2267–30 SAGO at U_G of 1.736 m/s.....	142
Figure 5.17: Effect of the mode of gas injection on the kinetic energy per unit mass (m^2/s^2) of SAGO with (i) uniform, (ii) two-jet, and (iii) single-jet gas distributor for binary mixtures of (a) 30 GB2267–70 SAGO, (b) 50 GB2267–50 SAGO, and (c) 70 GB2267–30 SAGO at U_G of 1.736 m/s.	143
Figure 5.18: Effect of the mode of gas injection on the total particle-particle drag force magnitude for binary mixtures of (a) 30 GB2267–70 SAGO, (b) 50 GB2267–50 SAGO, and (c) 70 GB2267–30 SAGO at U_G of 1.736 m/s.....	144
Figure 5.19: Effect of the mode of gas injection on the total kinetic energy per unit mass of GB2267 for (a) 30 GB2267–70 SAGO, (b) 50 GB2267–50 SAGO, and (c) 70 GB2267–30 SAGO at U_G of 1.736 m/s.....	145
Figure 5.20: Effect of the mode of gas injection on the total kinetic energy per unit mass of SAGO for (a) 30 GB2267–70 SAGO, (b) 50 GB2267–50 SAGO, and (c) 70 GB2267–30 SAGO at U_G of 1.736 m/s.....	146
Figure 5.21: Effect of the mode of gas injection on the mixing index for binary mixtures of (a) 30 GB2267–70 SAGO, (b) 50 GB2267–50 SAGO, and (c) 70 GB2267–30 SAGO at U_G of 1.736 m/s.	147
Figure 5.22: Effect of $\beta_{air} - GB$ model of (a) Gidaspow [66], (b) Gibilaro et al. [68], and (c) modified drag on the distribution of K.E of GB2267 for binary mixture of 50 GB2267–50 SAGO (Two-jet distributor, $U_G = 1.736$ m/s)	148

Figure 5.23: Effect of $\beta_{air} - GB$ model of (a) Gidaspow [66], (b) Gibilaro et al. [68], and (c) modified drag on the distribution of K.E of GB2267 for binary mixture of 70 GB2267–30 SAGO (Two-jet distributor, $U_G = 1.736$ m/s)	149
Figure 5.24: Effect of bed composition on the instantaneous volume fraction distribution of (a) GB2267 and (b) measurements (Black: GB2267, Green: SAGO, Red: Air) for binary mixture of (i) 70 GB2267–30 GB96, (ii) 50 GB2267–50 GB96, and (iii) 30 GB2267–70 GB96 (single-jet distributor, $U_G = 1.736$ m/s)	150
Figure 5.25: Effect of bed composition on the instantaneous volume fraction distribution of (a) GB and (b) measurements (Black: GB922, Grey: GB96) for binary mixture of (i) 70 GB922–30 GB96, (ii) 50 GB922–50 GB96, and (iii) 30 GB922–70 GB96.....	151
Figure 5.26: Comparison of measured and predicted height of segregated GB922 layer for 70 GB922–30 GB96 binary mixture at U_G of (a) 0.695 m/s and (b) 0.83 m/s (Binary mixture with $d_{pr} = 9$, $\rho_{pr} = 1$, Uniform distributor).....	153
Figure 5.27: Effect of bed composition on time-evolution of mixing index for binary mixture differing only in size (uniform distributor, U_G of 0.695 m/s)	153
Figure 5.28: Effect of the bed composition on the total local drag force/gravitational force for (a) 70 GB922–30 GB96, (b) 50 GB922–50 GB96, and (c) 30 GB922–70 GB96 binary mixtures at U_G of 0.695 m/s.....	154
Figure 5.29: Effect of the bed composition on the total local particle-particle drag force/gravitational force (Binary mixture with $d_{pr} = 9$, $\rho_{pr} = 1$, Uniform distributor, $U_G = 0.695$ m/s)	154
Figure 5.30: Effect of the mode of the gas-injection on the (i) predicted volume fraction distribution of GB922 and (ii) measurements (GB922: Black, GB96: Grey) for (a) uniform distribution and (b) two-jet distribution for 70 GB922–30 GB96 binary mixture differing in size at $U_G = 0.83$ m/s.....	156
Figure 5.31: Effect of mode of gas injection on the total (a) particle-particle drag force and (b) K.E of GB922 for 70 GB922–30 GB96 binary mixture at $U_G = 0.83$ m/s	156
Figure 5.32: Effect of bed composition on the instantaneous volume fraction distribution of (a) GB922 and (b) measurements (Black: GB, Green: SAGO, Red: Air) for binary mixture of (i) 70 GB922–30 SAGO, (ii) 50 GB922–50 SAGO, and (iii) 30 GB922–70 SAGO.....	157
Figure 5.33: Comparison of measured and predicted time-evolution of mixing index at $U_G = 1.04$ m/s (Binary mixture with $d_{pr} = 0.4$, $\rho_{pr} = 2$, uniform distributor)	157
Figure 6.1: (a) Illustration of fluidized bed gasifier used in present work (Karimipour et al. [137]) and (b) corresponding solution domain	166
Figure 6.2: Effect of the grid resolution on time-evolution of solids dispersion height.....	174
Figure 6.3: Effect of the grid resolution on bubble size distribution	175
Figure 6.4: Effect of the grid resolution on the time-evolution of the outlet mole fraction of (a) CO ₂ , (b) CO, (c) H ₂ , and (d) temperature of gas-mixture phase	175
Figure 6.5: Effect of the grid resolution on time-averaged mixture-gas temperature along the bed height ($m_{coal} = 0.036$ g/s)	176
Figure 6.7: Time-evolution of the (a) mole fraction of species at outlet and (b) heterogeneous reaction rates (m_{coal} of 0.036 g/s)	177
Figure 6.8: Comparison of measured [137] and predicted outlet syngas composition for m_{coal} of (a) 0.063 g/s, (b) 0.0495 g/s, and (c) 0.036 g/s.....	178

Figure 6.9: Effect of the model for $\beta_{gas} - inert$ on time-evolution of the (a) gas-inert solid phase momentum exchange coefficient and (b) relative velocity of coal and inert solid phases (m_{coal} of 0.036 g/s).....	180
Figure 6.10: Effect of the model for $\beta_{gas} - inert$ on bubble size distribution (m_{coal} of 0.036 g/s).....	180
Figure 6.11: Effect of the model for $\beta_{gas} - inert$ of (i) Gidaspow [38], (ii) Gibilaro et al. [52] and (iii) Li and Yang [59] on volume fraction distribution of (a) mixture-gas and (b) char (m_{coal} of 0.036 g/s).....	181
Figure 6.12: Effect of the model for $\beta_{gas} - inert$ on the solids dispersion height for m_{coal} of (a) 0.036 g/s and (b) 0.063 g/s.....	182
Figure 6.13: Effect of the model for $\beta_{gas} - inert$ on time-averaged axial char hold-up ...	182
Figure 6.14: Effect of the model for $\beta_{gas} - inert$ of (i) Gidaspow [38], (ii) Gibilaro et al. [52] and (iii) Li and Yang [59] on heterogenous reaction rate (mol/m ³ s) of (a) C+O ₂ →CO ₂ , (b) C+CO ₂ →2CO, (c) C+H ₂ O→CO+H ₂ , and (d) C+2H ₂ →CH ₄ at (a) 20 s and (b) 40 s (m_{coal} of 0.036 g/s).....	184
Figure 6.15: Effect of the model for $\beta_{gas} - inert$ of (i) Gidaspow [38], (ii) Gibilaro et al. [52] and (iii) Li and Yang [59] on temperature of gas phase (m_{coal} of 0.036 g/s).....	185
Figure 6.16: Effect of the model for $\beta_{gas} - inert$ on time-averaged axial temperature of coal (m_{coal} of 0.036 g/s).....	185
Figure 6.17: Effect of the model for $\beta_{gas} - inert$ of (i) Gidaspow [38], (ii) Gibilaro et al. [52] and (iii) Li and Yang [59] on mole fraction distribution of species at (a) 20 s and (b) 40 s.....	186
Figure 6.18: Effect of the model for $\beta_{gas} - inert$ on time-averaged axial species mole fraction of (a) CO ₂ , (b) CO, (c) H ₂ , and (d) H ₂ O (m_{coal} of 0.036 g/s).....	187
Figure 6.19: Effect of the bed operating temperature on the time-evolution of the water-gas shift reaction (m_{coal} of 0.036 g/s, $\beta_{gas} - inert$: Gidaspow [38]).....	189
Figure 6.20: Effect of model for $\beta_{gas} - inert$ on outlet syngas composition for inlet m_{coal} of 0.036 g/s.....	190
Figure 6.21: Effect of m_{coal} on bubble size distribution ($\beta_{gas} - inert$ model of Gibilaro et al. [52]).....	193
Figure 6.22: Effect of the model for $\beta_{gas} - inert$ of (i) Gidaspow [38], (ii) Gibilaro et al. [52] and (iii) Li and Yang [59] on volume fraction distribution of (a) mixture-gas and (b) char (m_{coal} of 0.063 g/s).....	194
Figure 6.23: Effect of the model for $\beta_{gas} - inert$ of (i) Gidaspow [38], (ii) Gibilaro et al. [52] and (iii) Li and Yang [59] on the heterogenous reaction rate (mol/m ³ s) (a) C+O ₂ →CO ₂ , (b) C+CO ₂ →2CO, and (c) C+H ₂ O→CO+H ₂ (m_{coal} of 0.063 g/s).....	195
Figure 6.24: Effect of model for $\beta_{gas} - inert$ on outlet syngas composition.....	196

List of Tables

Table 2.1: Properties of particles	15
Table 2.2: Unary and binary gas-solids systems considered in the present study	15
Table 2.3: Measured and calculated A_{SAGO}	19
Table 2.4: Incipient and final fluidization velocities of binary mixtures.....	23
Table 3.1: Superficial gas velocities and minimum fluidization velocities considered.....	49
Table 3.2: Eulerian model (conservation equations)	50
Table 3.3: Gas-solid drag closure models used in the present work.....	51
Table 3.4: Kinetic Theory of Granular Flow (KTGF) closure models	53
Table 3.5: Cumulative time-averaged gas-solid drag force per unit volume ($\text{kg/m}^2\text{s}^2$).....	61
Table 3.6: Cumulative time-averaged solid viscosities (Pa.s) (averaged over the computational cell with $\alpha s > 0$).....	66
Table 3.7: Correlations used to calculate the bubble diameter	70
Table 3.8: Cumulative (summed over entire domain) time-averaged velocity (m/s) of solid phase	80
Table 4.1: Applicability of closure models for a range of U_G/U_{mf}	89
Table 4.2: Particle-particle drag closure models used in the present work	90
Table 4.3: Initial packing limit of the solid phases	91
Table 4.4: Time-and volume-averaged (over entire domain) quantities.....	103
Table 4.5: Different Ps, f models and ϕ values used for the comparison	104
Table 4.6: Cumulative time-averaged drag force per unit volume ($\text{kg/m}^2\text{s}^2$).....	109
Table 5.1: Properties of the particles used in the binary mixtures.....	123
Table 5.2: Binary mixtures considered, operating $U_G, U_G/U_{if}, U_G/U_{ff}$, and packing limit of solid phases	125
Table 5.3: Closure models/parameters and operating conditions used for simulations of unary gas-solid flows	130
Table 5.4: Time-and volume-averaged quantities	155
Table 6.1: Eulerian model (conservation equations)	167
Table 6.2: Reactions considered	171
Table 6.3: Time-averaged (entire domain) drag quantities.....	179
Table 6.4: Effect of model for $\beta_{gas - inert}$ on time-averaged (entire domain) heterogeneous reaction rates	188
Table 6.5: Effect of model for $\beta_{gas - inert}$ on different parameters	192

Nomenclature

Notations

U_{mf}	minimum fluidization velocity (m/s)
U_{mb}	minimum bubbling velocity (m/s)
U_{fc}	critical fluidization velocity (m/s)
U_{if}	initial fluidization velocity (m/s)
U_{ff}	final fluidization velocity (m/s)
U_G	superficial gas velocity (m/s)
d_{pr}	size ratio (-)
d_s	diameter of particle (m)
d_b	diameter of bubble (cm)
h_s	dispersion height of solid (m)
W	width of the bed (m)
$U_{G,injection}$	injection gas velocity (m/s)
H_b	initial static bed height (m)
H_d	heterogeneity index (-)
$x_{flotsam}$	mass fraction of flotsam (-)
K_{fri}	coefficient of friction for long-term particle frictional contacts (-)
C_{fri}	coefficient of friction for short-term particle frictional contacts (-)
\overrightarrow{U}_g	velocity of gas phase (m/s)
\overrightarrow{U}_{s_i}	velocity of solid phase (m/s)
$\overrightarrow{U}_{s_i,w}$	velocity of i^{th} solid phase near the wall (m/s)
P_g	shared gas phase pressure (pa)
P_s^t	solid phase pressure (Pa)
p_s	solids pressure due to kinetic and collisional effects (pa)
$P_{s,f}$	solids frictional pressure (pa)
$e_{s,w}$	particle-wall normal restitution coefficient (-)
e_{ss}	particle-particle restitution coefficient (-)
$g_{0,ss}$	radial distribution function (-)
d_s	diameter of solid phase (m)
C_D	drag coefficient (-)
H_d	heterogeneity index (-)
S_{sg}	mass source term (kg/m ² s)
MW_{char}	molecular weight of char (kg/kmol)
$MW_{g,i}$	molecular weight of species 'i' in gas mixture-gas (kg/kmol)
$Y_{g,i}$	species in gas phase (-)
$Y_{s,i}$	species in solid phase (-)
$R_{s,i}$	heterogeneous reaction rate (kmol/m ³ s)

$R_{g,i}$	homogenous reaction rate (kmol/m ³ s)
T	temperature of the gas phase (k)
R	universal gas constant (J/kmol.K)
\bar{g}	gravity acceleration (m/s ²)
\bar{I}	identity matrix
I_{2D}	second order stress tensor (s ⁻¹)
H_g	enthalpy of gas phase (J/kg)
H_{s_i}	enthalpy of i th solid phase (J/kg)
H_i	enthalpy of species 'i' (J/kg)
$C_{p,i}$	specific heat of species 'i' (J/kg.K)
$\Delta H_{f,i}$	heat of formation (J/kg)
h_{gs_i}	heat transfer coefficient between gas and i th solid phase (W/m ² K)
$J_{g,i}$	diffusion flux of species 'i' (1/m ² s)
$D_{i,j}$	binary mass diffusion coefficient (m ² /s)
Nu_s	Nusselt number (-)
Re_s	Reynolds number of solid phase (-)
Sc_t	Schmidt number (-)

Greek symbols

Φ_s	sphericity (-)
σ^2	variance (-)
σ_s^2	variance of a phase when the bed is completely segregated (-)
σ_M^2	variance of a phase when the bed is completely mixed (-)
α_g	volume fraction of gas-phase (-)
α_{s_i}	volume fraction of i th solid phase (-)
α_{s_k}	volume fraction of k th solid phase (-)
$\alpha_{s,min}$	minimum frictional packing limit (-)
$\alpha_{s,max}$	maximum frictional packing limit (-)
ρ_{pr}	diameter ratio (-)
ρ_g	density of gas-phase (kg/m ³)
ρ_{s_i}	density of i th solid phase (kg/m ³)
$\rho_{s,i}$	density of species 'i' in mixture-solid (kg/kmol)
$\bar{\tau}_g$	gas phase stress tensor (pa)
$\bar{\tau}_{s_i}$	i th solid phase stress tensor (pa)
$\bar{\tau}_{s_i,w}$	wall shear stress of i th solid phase (pa)
β_{gs}	momentum exchange coefficient between gas phase and solid phase (kg/m ³ s)
$\beta_{s_i s_k}$	momentum exchange coefficient between i th solid phase to k th solid phase (kg/m ³ s)
β_{pec}	peculiar particle–particle drag coefficient (kg/m ³ s)
β_{hyd}	fluid-dynamic particle–particle drag coefficient (kg/m ³ s)
β_{fri}	frictional particle–particle drag coefficient (kg/m ³ s)

μ_s	viscosity of solid phase (pa.s)
μ_g or μ_{gl}	viscosity of gas phase (pa.s)
μ_{gt}	turbulent viscosity of gas phase (pa.s)
$\mu_{s,col}$	collisional viscosity of solid phase (pa.s)
$\mu_{s,kin}$	kinetic viscosity of solid phase (pa.s)
$\mu_{s,fr}$	frictional viscosity of solid phase (pa.s)
λ_{sb}	bulk viscosity of solid phase (pa.s)
λ_s	thermal conductivity of gas phase (W/m.K)
λ_g	thermal conductivity of gas phase (W/m.K)
$\lambda_{s,i}$	thermal conductivity of species 'i' in solid phase (W/m.K)
$\lambda_{g,i}$	thermal conductivity of species 'i' gas phase (W/m.K)
θ_s	granular temperature of solid phase (m^2/s^2)
κ_θ	diffusional coefficient of granular temperature of solid phase (kg/ms)
γ_θ	collisional dissipation of energy of solid phase (kg/ms^3)
γ_{char}	stoichiometric coefficient (-)
ϕ	particle-wall tangential restitution coefficient also termed as specular coefficient (-)
φ	switch function
κ	turbulent kinetic energy (m^2/s^2)
ε	rate of dissipation of turbulent kinetic energy (m^2/s^3)

Acronyms

CFD	computational fluid dynamics
DEM	discrete element method
ECT	electrical capacitance tomography
TFM	two fluid model
MFM	multi fluid model